

Article

Relationships between Abyssal Redox Conditions and Rock Magnetic Properties of Surficial Sediments in the Western Pacific

Yanping Chen ^{1,†}, Dong Xu ^{2,†}, Huafeng Qin ^{3,4}, Geng Liu ^{3,4}, Yibing Li ⁵, Weiwei Chen ⁵ and Liang Yi ^{5,*} 

¹ Zhejiang Academy of Marine Sciences, Second Institute of Oceanography, Ministry of Natural Resources, Hangzhou 310012, China; chenai0812@163.com

² MNR Key Laboratory of Submarine Geosciences, Second Institute of Oceanography, Ministry of Natural Resources, Hangzhou 310012, China; xudongsio@126.com

³ State Key Laboratory of Lithospheric Evolution, Institute of Geology and Geophysics, Chinese Academy of Sciences, Beijing 100029, China; huafeng_qin@mail.iggcas.ac.cn (H.Q.); gengliu1995@outlook.com (G.L.)

⁴ University of Chinese Academy of Sciences, Beijing 100049, China

⁵ State Key Laboratory of Marine Geology, Tongji University, Shanghai 200092, China; yibing_l@163.com (Y.L.); sww@tongji.edu.cn (W.C.)

* Correspondence: yiliang@tongji.edu.cn

† These authors contributed equally to this work.

Abstract: Reconstructing changes in deep/bottom-water redox conditions are critical for understanding the role of the deep ocean in global carbon and metals cycling; nevertheless, the quantitative relationships between redox proxies and abyssal dissolved oxygen are poorly investigated. In this work, we studied the rock magnetic properties of surficial sediments in the western Pacific to investigate their relationship with regional redox conditions. Our results reveal a consistent sedimentary magnetic mineral assemblage in the western Pacific, dominated by pseudo-single-domain magnetite (Fe₃O₄), while the ratio of detrital and biogenic magnetite particles in different sites varies substantially. Detailed analyses identified two major magnetic-coercivity components, with modal coercivity values of 13.1 ± 1.6 mT and 54.7 ± 5.3 mT, respectively. All the magnetic parameters we measured, including both concentration-dependent and grain-size-dependent parameters, and the magnetic coercivities, are generally correlated to sedimentary redox conditions; however, the coercivities obtained by mathematical unmixing exhibit a stronger linkage, explaining about a quarter of variance of redox changes. Our findings confirm the potential of magnetic properties for tracing abyssal redox changes in the western Pacific, while the observed magnetic-redox relationships are complex and need further investigation.

Keywords: deep-sea sediments; magnetic properties; magnetic coercivity; redox changes; western Pacific



Citation: Chen, Y.; Xu, D.; Qin, H.; Liu, G.; Li, Y.; Chen, W.; Yi, L. Relationships between Abyssal Redox Conditions and Rock Magnetic Properties of Surficial Sediments in the Western Pacific. *J. Mar. Sci. Eng.* **2023**, *11*, 1132. <https://doi.org/10.3390/jmse11061132>

Academic Editor: Dmitry A. Ruban

Received: 8 April 2023

Revised: 25 May 2023

Accepted: 26 May 2023

Published: 27 May 2023



Copyright: © 2023 by the authors. Licensee MDPI, Basel, Switzerland. This article is an open access article distributed under the terms and conditions of the Creative Commons Attribution (CC BY) license (<https://creativecommons.org/licenses/by/4.0/>).

1. Introduction

Redox conditions are a critical environmental factor in paleoceanography, e.g., [1–4], representing a key interaction point between various climatic system components, such as oceanic water masses, marine productivity, and sediment fluxes. To reconstruct the past changes in redox conditions, the proxies are mainly based on geochemical properties of foraminiferal shells or deep-sea sediments. For example, for Cenozoic sediments, the geochemical properties of benthic foraminifera are often employed. One of the most-used proxies is the stable carbon isotope composition ($\delta^{13}\text{C}$) and its inter-basinal gradient ($\Delta\delta^{13}\text{C}$), e.g., [5–7]. Carbon isotopes in ocean water are associated with the balance between dissolved inorganic and organic carbon, linked to deep-sea ventilation and thus redox conditions [8], while other studies have indicated that seawater temperature and carbon species have more influence on benthic $\delta^{13}\text{C}$ [9,10]. Trace elements in foraminifera and/or

sediments, including Mn, Zn, Ni, and V, e.g., [1,11,12], generally migrate from oxidizing to reducing environments; however, migration in the opposite direction may also occur, in the case of authigenic uranium, e.g., [3,13] and some rare earth elements (Ce, Y, and Ho), e.g., [14,15]. Thus, these trends reflect changes in redox conditions. Sedimentary and/or foraminiferal neodymium isotopes ($^{143}\text{Nd}/^{144}\text{Nd}$) are also used to trace redox changes, e.g., [16,17], because different water masses have distinct neodymium isotope patterns [18], which reflect changes in deep-sea ventilation and redox conditions. However, most present studies using the geochemical properties of foraminiferal shells or abyssal sediments are qualitative or semiquantitative, and there is a lack of quantitative tests, partially due to the high time- and expense-cost of geochemical measurements.

As a proxy that can be rapidly and easily measured, the magnetic properties of deep-sea sediments were recently proposed to be associated with deep-water redox conditions, e.g., [19–26]. Magnetic minerals are redox sensitive, due to conversions between Fe^{2+} and Fe^{3+} in crystal lattices, as in the cases of magnetite, maghemite, hematite, and iron sulfides (greigite or pyrrhotite). For example, experimental investigations of magnetic particles with different oxidation states showed that pseudo-single-domain (PSD) magnetite was significantly negatively correlated to partial oxidation in a shell-only model [27]. Thus, either in paleoenvironmental or experimental contexts, the potential of magnetic properties for reconstructing deep-sea redox conditions has been proposed. Nevertheless, there are few quantitative evaluations of magnetic properties–redox relationships using sediment samples covering a large region.

Given the absence of carbonate fossils beneath the carbonate compensation depth, which comprises a large area of the Pacific, it is important to further develop sedimentary proxies for deep-sea oxidation conditions. To this end, we compared the spatial distribution of the magnetic properties of bottom sediments from the western Pacific with abyssal (sedimentary) oxidation conditions in this study.

2. Materials and Methods

2.1. Study Sites

Sediment samples from 66 sites were collected in the western Pacific (Figure 1) in October 2017, using a box corer. The samples were obtained from the depth range of 2630–6060 m, and the sediments were predominantly light-brown to brown muds. The redox potential (Eh value) of the sediments was immediately measured on board, using a portable pH meter (INESA Co., PHBJ-260). Since the measurements were conducted in an on-board lab, the obtained Eh values may not directly represent the real ones of the deep-sea environment, but instead a proxy of sedimentary redox conditions.

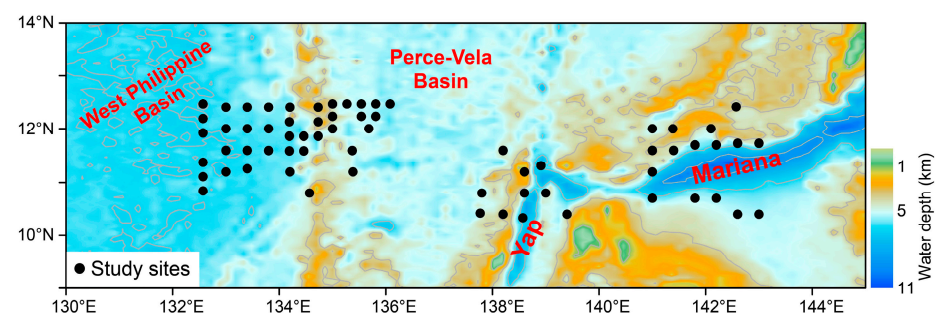


Figure 1. Schematic map showing the study area and study sites. Mariana, Mariana Trench; Yap, Yap Trench. The site information is listed in Table 1.

Table 1. The information of the 66 study sites.

Sites	Longitude (°E)	Latitude (°N)	Water Depth (m)	Sites	Longitude (°E)	Latitude (°N)	Water Depth (m)
A14	137.77	10.42	4690	E04	133.80	12.00	5720
A15	138.20	10.40	4200	E07	135.00	12.00	4620
A16	138.57	10.33	5990	E09	135.68	12.00	4750
A18	139.40	10.40	3890	E22	141.00	12.00	4070
J01A	142.28	10.35	4430	E23	141.38	12.00	2630
A27	142.60	10.40	4920	E25	142.10	12.00	4120
B06	134.57	10.80	4025	F02	133.00	12.40	5540
B14	137.80	10.80	4230	F03	133.40	12.40	5850
B16	138.60	10.80	5340	F04	133.80	12.40	5220
B17	139.00	10.80	3540	F05	134.20	12.40	5180
B22	141.00	10.70	5605	F26	142.57	12.41	3560
B24	141.80	10.70	4800	G01	132.57	12.46	5830
B25	142.20	10.70	5090	G09	134.73	12.40	3390
C02	133.00	11.20	5720	G10	135.00	12.46	4040
C03	133.40	11.26	5710	G11	135.27	12.46	4610
C05	134.20	11.20	5330	G12	135.54	12.46	4880
C08	135.38	11.20	4200	G13	135.81	12.46	5041
C16	138.60	11.20	3120	G14	136.08	12.46	5063
C17	138.91	11.32	5670	G15	132.57	12.19	6060
C22	141.00	11.20	4780	G21	134.19	12.13	5020
D02	133.00	11.60	5950	G23	134.73	12.13	3430
D03	133.40	11.60	5630	G24	135.00	12.23	3680
D04	133.80	11.60	5230	G26	135.54	12.23	4770
D08	135.37	11.60	4260	G27	135.81	12.23	5100
D15	138.20	11.60	4180	G28	132.57	11.92	5970
D22	141.00	11.60	3310	G34	134.19	11.86	5510
D23	141.40	11.60	4100	G35	134.46	11.86	3330
D24	141.80	11.70	5370	G36	134.73	11.86	4940
D25	142.20	11.70	5590	G46	134.19	11.59	5580
D26	142.60	11.73	5020	G47	134.46	11.59	4750
D27	143.00	11.73	3960	G51	132.57	11.38	5770
E02	133.00	12.00	5880	G57	132.57	11.11	5820
E03	133.40	12.00	5640	G60	132.57	10.84	5790

2.2. Magnetic Measurements

For the measurement of magnetic properties, the samples collected from the 66 sites were dried in vacuum and then packed in 8 cm³ cubic plastic boxes. Magnetic susceptibility was measured using an AGICO MFK1-FA Multi-Frequency Kappabridge magnetic susceptibility meter, at frequencies of 976 Hz and 15,616 Hz (χ_{LF} and χ_{HF} , respectively). Anhysteretic remanent magnetization (ARM) was imparted using a peak alternating field (AF) of 100 mT and a direct biasing field of 0.05 mT using a 2G Enterprises SQUID magnetometer with inline AF coils. The susceptibility of ARM (χ_{ARM}) was calculated as ARM/0.05 mT. Isothermal remanent magnetization (IRM) was imparted with a 2G Enterprises model 660 pulse magnetizer, with successive pulsed fields of 1 T (saturation IRM, SIRM), −0.1 T (IRM_{−0.1T}), and −0.3 T (IRM_{−0.3T}). The temperature-dependent magnetic susceptibilities (χ -T curves) were measured by continuous exposure of samples through temperature cycles from room temperature to 700 °C and back to room temperature in an argon atmosphere, using a Kappabridge KLY-3 with a CS-3 high-temperature furnace (Agico Ltd., Brno, Czech Republic). These measurements were conducted in the State Key Laboratory of Marine Geology, Tongji University.

The percentage frequency-dependent magnetic susceptibility (χ_{fd}), and S_{ratio} were calculated as $\chi_{fd} = \frac{\chi_{LF} - \chi_{HF}}{\chi_{LF}} \times 100\%$ and $S_{ratio} = -\frac{IRM_{-0.3T}}{SIRM} \times 100\%$, respectively. To assess the extent of early diagenetic alteration of the magnetic minerals, hysteresis loops and IRM acquisition curves were measured on all samples, using a MicroMag 3900 Vibrating Sample

Magnetometer (VSM, Princeton Measurements Inc., Westerville, OH, USA), with a peak field of 0.3 T. Saturation magnetization (M_s), saturation remanence (M_{rs}), coercive force (B_c), and the coercivity of remanence (B_{cr}) were determined from the hysteresis loops, after correction using the data between 0.25 and 0.30 T.

The mathematical unmixing of hysteresis loops and IRM acquisition curves can provide detailed information about different coercivity spectra [28]. A series of target functions have been proposed for unmixing [29]. We used the normal function to identify the potential end members of magnetic minerals in the sediments [29,30].

The polymodal distribution for unmixing in this study is expressed as follows:

$$F = p_1 f_1 + \dots + p_i f_i; \sum_1^n p_i = 1 \tag{1}$$

where f_i represents the function for component i where $i = 1$ to n components, and p_i is the percentage contribution of components. The normal function has the following form:

$$= p_1 \frac{1}{\sqrt{2\pi\alpha_1}} e^{-\left[\frac{(x-\beta_1)^2}{2\alpha_1^2}\right]} + (1 - p_1) \frac{1}{\sqrt{2\pi\alpha_2}} e^{-\left[\frac{(x-\beta_2)^2}{2\alpha_2^2}\right]} \tag{2}$$

Here, x is the independent variable and represents the magnetic field (IRMs on a logarithmic scale), and the dependent variables are the first and second derivatives of the IRM acquisition and hysteresis loop data, respectively, which were first standardized to the interval of [0, 1]. The coefficient p represents the relative ratio between two components (namely cont1 and cont2), α determines the distribution shape, and β controls the position of the central tendency of the curve, herein, the magnetic coercivity (namely Coe1 and Coe2).

First-order reversal curves (FORCs) were determined for five representative samples, setting a peak field of 1.0 T and an interval of 3.2 mT. To further characterize the magnetic minerals, a magnetic extract was obtained from a representative sample (from Site J01A) and used for transmission electron microscope (TEM) analysis, with a JEOL JEM2100F LaB6. These measurements were conducted in the Paleomagnetism and Geochronology Lab (PGL), Institute of Geology and Geophysics, Chinese Academy of Sciences.

3. Results

3.1. Relationships between Magnetic Parameters

As shown in Table 2, the mass-specific χ_{LF} of the samples varies from $1.4 \times 10^{-7} \text{ m}^3/\text{kg}$ to $7.8 \times 10^{-6} \text{ m}^3/\text{kg}$, and χ_{fd} is generally high (>5%) and variable (mean and standard deviation of $8.2 \pm 7.2\%$). χ_{ARM} is sensitive to single domain (SD) grains [31,32], and SIRM reflects the content of the remanence-bearing fraction, and it excludes the influence of superparamagnetic (SP) grains [33]. The ranges for χ_{ARM} and SIRM are 3.8×10^{-7} – $6.7 \times 10^{-5} \text{ m}^3/\text{kg}$ and 0.28 – $9.6 \times 10^{-3} \text{ Am}^2/\text{kg}$, respectively.

Table 2. Statistic properties of magnetic parameters of the 66 study sites.

	Units	Min	Max	Mean	Standard Deviation	Skewness	Kurtosis
χ_{LF}	m^3/kg	1.4×10^{-7}	7.8×10^{-6}	1.9×10^{-6}	1.4×10^{-6}	1.5	3.6
χ_{HF}	m^3/kg	1.2×10^{-7}	7.5×10^{-6}	1.8×10^{-6}	1.4×10^{-6}	1.5	3.4
χ_{fd}	%	1.1	33.1	8.2	7.2	2.1	4.0
χ_{ARM}	m^3/kg	3.8×10^{-7}	6.7×10^{-5}	1.2×10^{-5}	1.1×10^{-5}	2.8	10.8
SIRM	Am^2/kg	2.8×10^{-4}	9.6×10^{-3}	2.8×10^{-3}	1.9×10^{-3}	1.0	1.2
IRM _{0.1T}	Am^2/kg	1.6×10^{-4}	4.7×10^{-3}	1.8×10^{-3}	1.3×10^{-3}	0.7	−0.6
IRM _{0.3T}	Am^2/kg	2.7×10^{-4}	9.4×10^{-3}	2.7×10^{-3}	1.9×10^{-3}	1.0	1.1

The concentration-dependent magnetic parameters (χ , χ_{ARM} , and SIRM) show similar variations. Considering the general relationships between the magnetic parameters

(Figure 2, Table 3), we suppose that there are no significant differences in magnetic properties (hence in magnetic mineral sources) between the study sites. However, the large variations of the concentration-dependent magnetic parameters indicate large differences in the magnetic mineral content of these sediments, suggesting that the dataset may be broadly representative of the bottom sediments in the western Pacific.

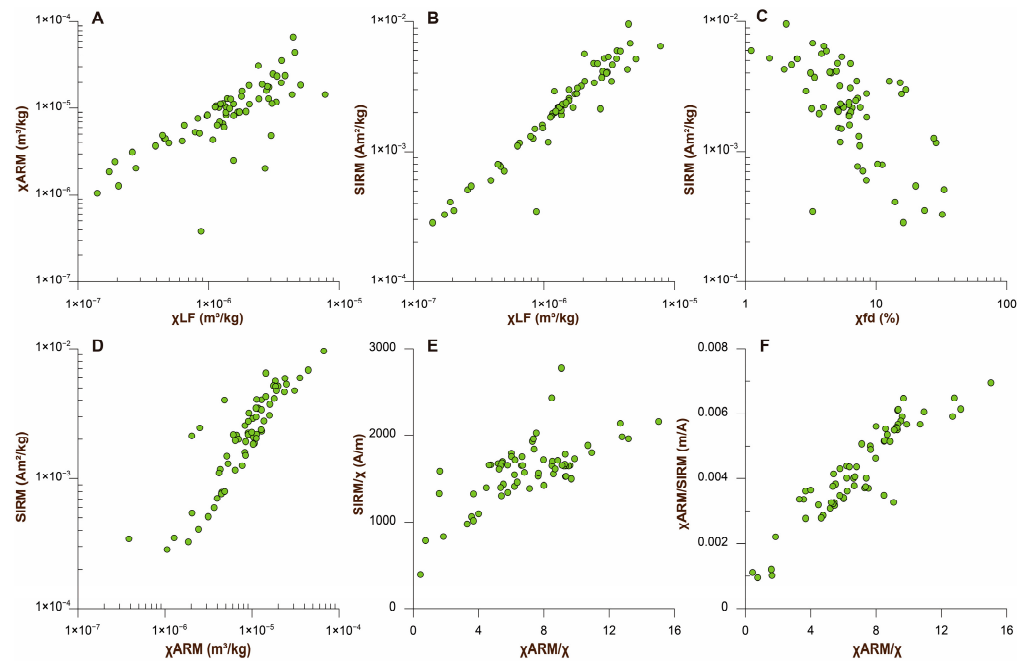


Figure 2. Scatterplot of the relationships between selected magnetic parameters (A–F). It is noted that there were in total 66 samples analyzed.

Table 3. Correlation coefficients between chemical elements of the 66 study sites.

	χ_{LF}	χ_{fd}	χ_{ARM}	SIRM	χ_{ARM}/χ	SIRM/ χ
χ_{LF}	1					
χ_{fd}	−0.48	1				
χ_{ARM}	0.64	−0.38	1			
SIRM	0.88	−0.51	0.87	1		
χ_{ARM}/χ	−0.32	0.32	0.34	−0.04 ¹	1	
$\chi_{ARM}/SIRM$	−0.22 ¹	0.24 ¹	0.36	−0.04 ¹	0.91	1
SIRM/ χ	−0.38	0.25	0.14 ¹	0.57	0.69	0.39

¹ All coefficients are significant at $p < 0.05$ level, except for these five values. The correlation coefficients are all based on a linear relationship.

3.2. Spatial Distribution of Magnetic Parameters

The consistency of magnetic properties between the sites in the western Pacific offers the opportunity to visualize the spatial pattern of individual magnetic parameters and to compare them with the Eh values.

As can be seen in Figures 3 and 4, the Eh values are relatively high in the West Philippine Basin and the Parece Vela Basin and low at the sites from the Yap and Mariana trenches. The spatial pattern of the Eh values can be attributed to the generally deeper water depths of the study sites in the two basins, where the dissolved oxygen levels are maintained by the Antarctic bottom water (AABW) [34,35] and/or the unique submarine topography [36,37].

For the concentration-dependent magnetic parameters (χ , χ_{ARM} , and SIRM), high values occur in the vicinity of the two trenches, while in the two basins, relatively low values are found (Figure 3). The cause of this spatial pattern can partially be attributed to

water depth, since shallower sites in the western Pacific may be more influenced by marine productivity in the upper ocean layer, e.g., [37–39].

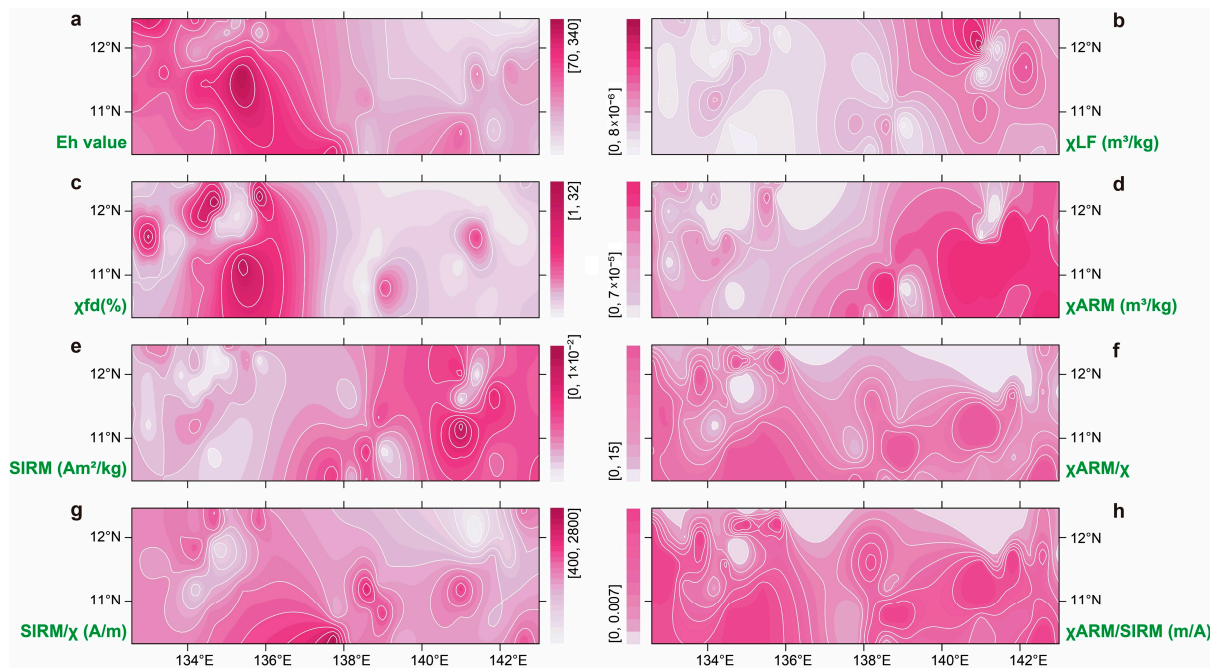


Figure 3. Spatial distribution of Eh values and the selected magnetic parameters (a–h).

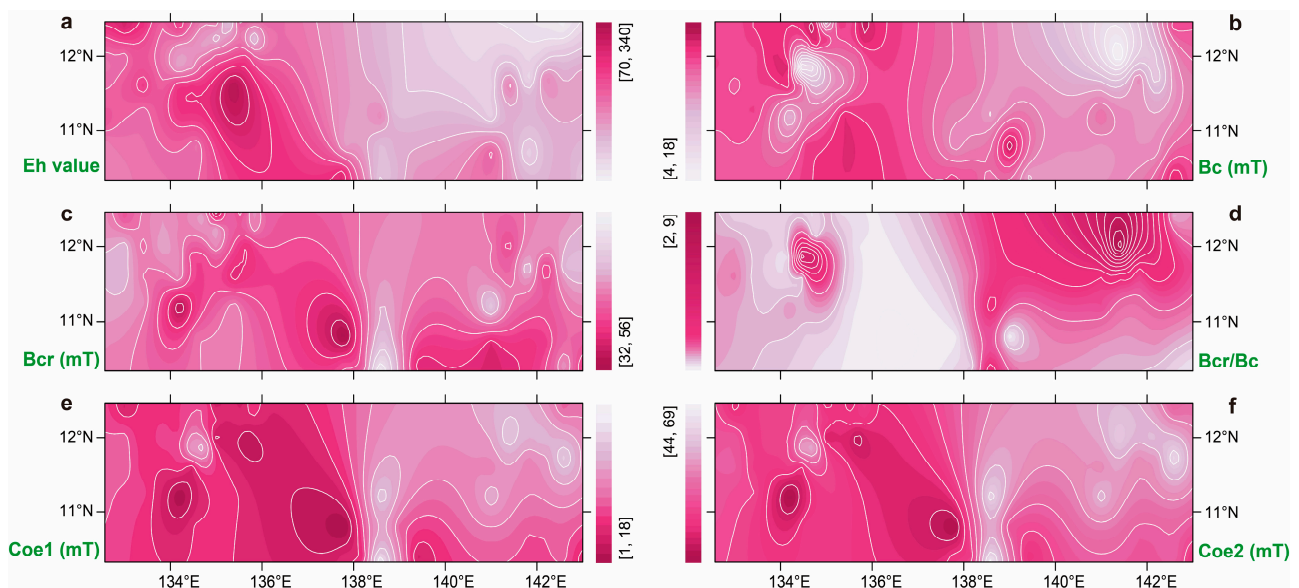


Figure 4. Spatial distribution of Eh value, Bcr/Bc, and magnetic coercivities (a–f). Note that the scales in (c,e,f) are reversed.

For the grain-size-dependent rock magnetic parameters (χ_{fd} , χ_{ARM}/χ , SIRM/ χ , and $\chi_{ARM}/SIRM$), no consistent spatial pattern is evident (Figure 3), potentially indicating a complex response of the magnetic grain size to specific regional settings. However, a similarity between magnetic coercivities and Eh is observed (Figure 4), that is, coercivity values are relatively high in the Yap and Mariana trenches, but low in the two basins. This spatial pattern of magnetic coercivity in abyssal sediments is consistent with the results of experimental studies, e.g., [27], which generally indicate that the magnetic properties of PSD magnetite are sensitive to early stage oxidation.

3.3. Sedimentary Magnetic Mineralogy

The magnetic hysteresis loops are closed below 200 mT (Figure 5a), and the IRM acquisition curves are saturated in relatively low magnetic fields (<200 mT) (Figure 5d), with S_{ratio} values of 0.945–0.998, indicating that these sediments are dominated by low-coercivity magnetic minerals.

The B_c and B_{cr} values are 13.5 ± 2.7 mT and 43.7 ± 4.2 mT (Table 4), respectively, and on the Day plot [40], they are distributed within the PSD range (Figure 5c). A two-humped distribution of the normal function was applied to mathematically unmix the hysteresis loops [29,30], and their coercivities (Co_{e1} and Co_{e2}) are 13.1 ± 1.6 mT and 54.7 ± 5.3 mT, respectively (Figure 5b; Table 4). The two-humped distribution in the log-normal function was also applied to unmix the IRM acquisition curves [41]. There is no significant difference in the Co_{e2} values between the hysteresis-loop-based and IRM-acquisition-based results ($r = 0.58$, $p < 0.01$) (Figure 5e), confirming the reliability of the mathematical unmixing. In addition, in χ - T heating curves, a gradual decrease in magnetic susceptibility till ~ 580 °C was observed (Figure 5g–i).

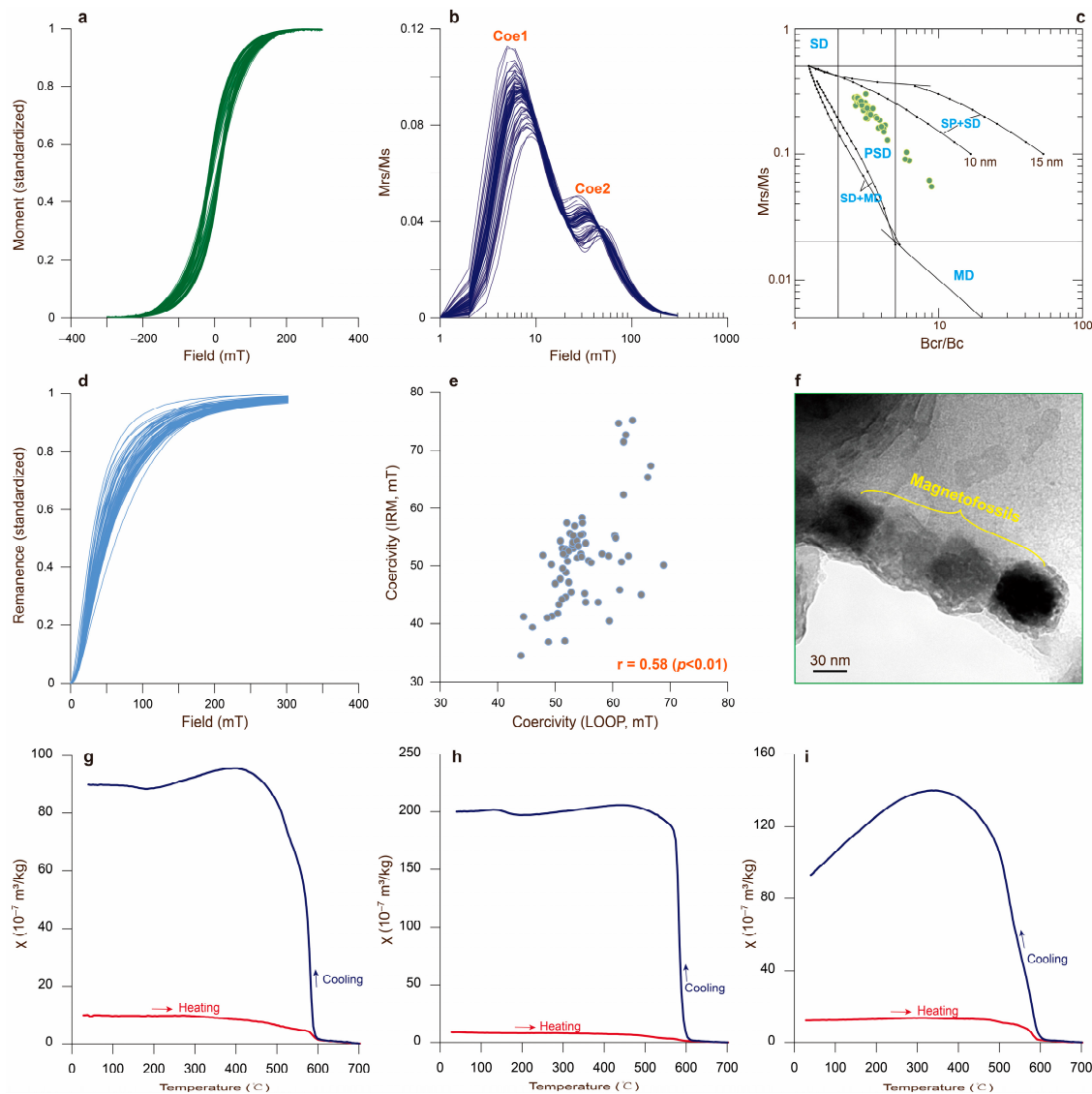


Figure 5. Rock magnetic properties of the bottom sediment samples from the western Pacific. (a) Hysteresis loops (calibrated). (b) Mathematical unmixing of the second-order derivative of the

hysteresis loops showing two coercivity components (Coe1 and Coe2). (c) Day plot [42,43]. SD, single domain; MD, multidomain; PSD, pseudo-single-domain; SP, superparamagnetic. (d) IRM acquisition curves. (e) Comparison between the hysteresis-loop-based and IRM-acquisition-based results. It is noted that there were in total 66 samples analyzed in (a,d). (f) TEM image of probable magnetofossils (Site J01A, Mariana Trench). (g–i) χ -T curves of sites E03 (West Philippine Basin), C16 (Yap Trench), and J01A (Mariana Trench), respectively.

Table 4. Statistic properties of loop parameters of the 66 study sites.

	Units	Min	Max	Mean	Standard Deviation	Skewness	Kurtosis
Bc	mT	4.5	17.1	13.5	2.7	−1.4	1.9
Bcr	mT	32.0	55.5	43.6	4.2	−0.6	1.2
Mrs/Ms	-	0.055	0.29	0.22	0.05	−1.3	1.3
Cont1	%	49.2	57.7	52.8	2.1	0.6	−0.2
Coe1	mT	9.9	17.7	13.1	1.6	0.7	0.3
Cont2	%	42.3	50.8	47.2	2.1	−0.6	−0.2
Coe2	mT	44.0	68.9	54.7	5.3	0.6	0.1

Additionally, there is a transition from a large vertical spread to a more limited spread in the contours in the FORC diagrams (Figure 6), with most of the coercivity distribution within the range of 10–60 mT, and a peak at ~20 mT. The limited vertical spread and wide horizontal spread of the contours (Figure 6d,e) indicate minimal magnetostatic interactions [44,45], which is in agreement with comparable rock magnetic results from the Mariana Trench [46] and the West Philippine Basin [36].

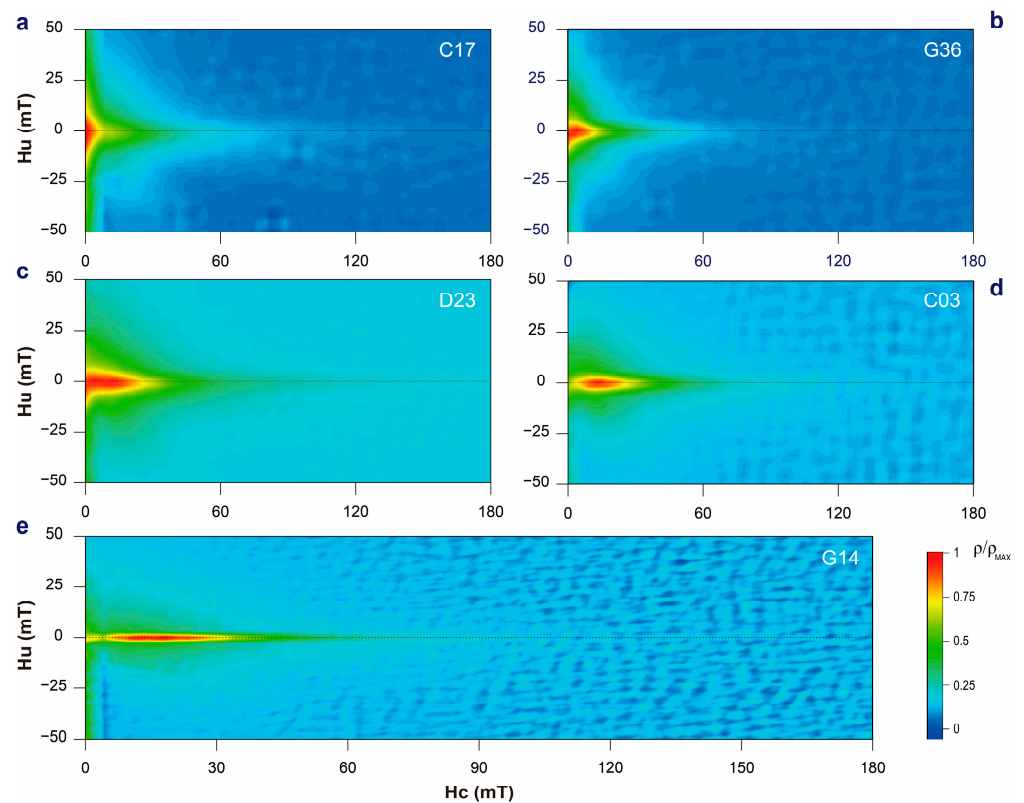


Figure 6. FORC diagram for five representative samples. All diagrams were produced using the FORCme software with a smoothing factor of 3. Sample G14 (e) was subjected to high-resolution FORC analysis (360 lines), while for the other samples (a–d), a standard analysis was conducted (90 lines).

The observed magnetic characteristics of the study sites are similar to those of cores NGC36, NGC65, and NGC88 from the western Pacific [38], core MABC-11 from the Magellan Seamount [37], and core XTGC1311 from the middle Pacific [47], for which the presence of the magnetofossils from magnetic bacteria were claimed. The TEM investigation of Site J01A (Figure 5f) shows a chain-like shape of magnetic minerals, confirming that magnetofossils are widespread in the abyssal sediments of the western Pacific. Thus, we propose that the transition in the FORC distribution evident in Figure 6a–e likely represents an increase in the content of magnetofossils in the sediments.

4. Discussion

Integrating the foregoing observations with previous studies in this region [11,38,39,46,48], it is inferred that magnetite (Fe_3O_4) is the dominant magnetic mineral in studied sediments, and that our samples are representative of the magnetic properties of the bottom sediments of the western Pacific. Thus, they offer the opportunity to test the relationship between deep-water redox conditions and sediment magnetic properties (Figure 7).

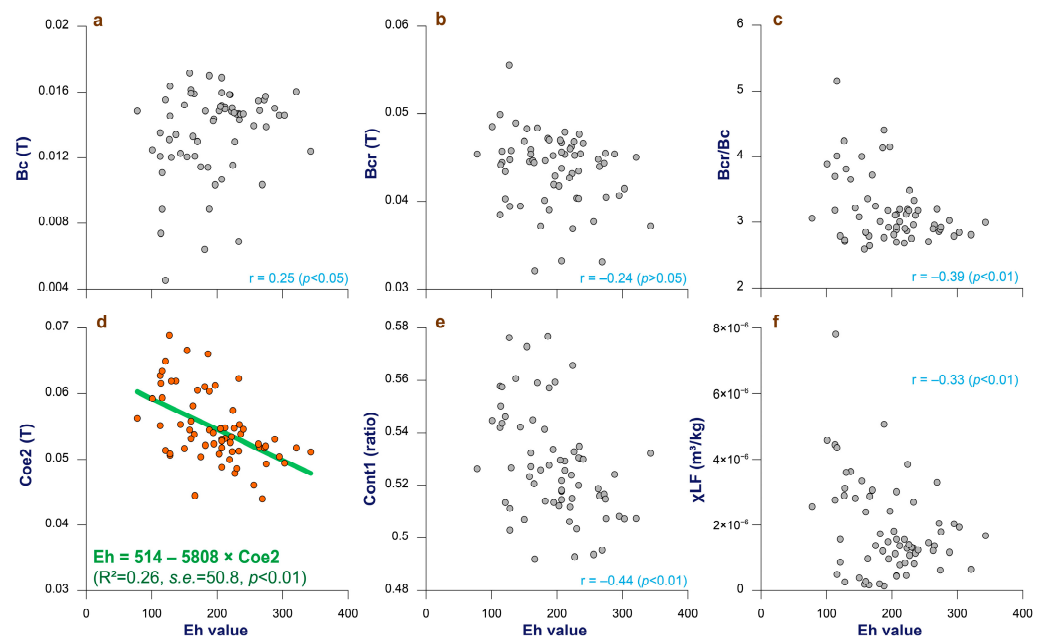


Figure 7. Results of regression analysis between selected rock magnetic parameters and deep-sea redox conditions (Eh value). Correlation coefficients are included in all plots (a–f), and the best-fit regression line is shown in (d).

The relationship is weak between Eh and Bc and Bcr, which is only significant at the 0.05 level (Figure 7a,b). This weak correlation suggests that redox conditions were not the only factor significantly influencing the bulk magnetic coercivity, and that other factors may include different proportions of magnetite grains with different coercivities. This inference is supported by the higher correlation between Eh and Coe2 and Cont1 (Figure 7d,e). In addition, different grain sizes of magnetic minerals may have different behaviors responding to oxidation [27], which could explain a weak correlation between Eh and Bcr/Bc (Figure 7c), since the Bcr/Bc ratio can be a proxy of magnetic grain size [49], like χ_{fd} , χ_{ARM}/χ , SIRM/ χ , and χ_{ARM}/SIRM .

We then conducted stepwise linear regression analysis of these magnetic parameters, and only the parameter Coe2 was retained in the analysis (Figure 7d). The regression results confirm the relationship between magnetic coercivity and deep-sea redox conditions; specifically, for PSD magnetite, the higher the deep-water oxidation status, the lower the coercivity, and vice versa. In this case, the partial oxidation of the exterior of PSD magnetite grains could reduce the effective diameter and thus reduce the coercivity [27,50].

It is noteworthy that Coe2 only explains ~25% of the variance in Eh values (Figure 7d), and that the coercivity variations are certainly affected by other factors, such as the magnetic grain size, mineralogy, and concentration. It is then suggested magnetic inference for redox conditions cannot be singly made without other evidence.

In addition, the topmost sediments on the seafloor in the western Pacific are typically modern-deposited, while some sites could be affected by random hiatuses [36,51]. Thus, in some cases, the measured samples may contain sediments spanning tens of thousands of years. For those samples, long-term exposure of bottom sediments to oxygen-rich bottom water may have resulted in the prolonged magnetization of magnetite grains from the shell to the core. In a shell–core modeling study, changes in the coercivity of magnetic grains were positively correlated to the degree of oxidation [27]. Because of this factor, sediments of different ages may represent a source of noise which affects the relationship between magnetic coercivity and deep-water redox conditions.

5. Conclusions

We have studied the rock magnetic properties of surficial sediments collected from 66 sites in the western Pacific, with the objective of investigating the relationship between magnetic properties and abyssal redox conditions. The principal results are as follows: (1) Magnetite with PSD magnetic behavior is inferred to be the dominant magnetic mineral in the sediments, and it may have both detrital and biogenic sources. (2) There are no significant differences in the relationships between the measured magnetic parameters. (3) Two major magnetic-coercivity components are identified, with modal coercivity values of 13.1 ± 1.6 mT and 54.7 ± 5.3 mT, respectively. These components are comparable between hysteresis loops and IRM acquisition curves. Based on these results, we infer that these two magnetic components occur consistently in the bottom sediments across the western Pacific, although their relative proportions vary substantially. All the rock magnetic parameters we measured, including those related to the concentration, grain size, and mineralogy, as well as the magnetic coercivity, are generally correlated to deep-sea sedimentary redox conditions (Eh value), implying a complex connection for magnetic properties. Moreover, coercivities obtained by mathematical unmixing have a significantly negative linkage to redox conditions, accounting for 26% of total variance in redox changes, possibly implying that the partial oxidation could reduce the effective diameter of PSD magnetite grains. Overall, our results demonstrate the potential of magnetic properties of deep-sea sediments in the western Pacific as a convenient and easily measured proxy for changes in sedimentary redox conditions; however, in practice, their use should be validated by other redox indicators.

Author Contributions: Conceptualization and methodology, L.Y.; sample collection D.X.; measurements Y.C., Y.L., G.L. and W.C.; formal analysis, L.Y. and H.Q.; original draft preparation, Y.C. All authors contributed to the data interpretation and provided significant input into the final manuscript. All authors have read and agreed to the published version of the manuscript.

Funding: This research was funded by National Natural Science Foundation of China, grant number 42177422, and National Programme on Global Change and Air-Sea Interaction, grant number GASI-04-HYDZ-02.

Institutional Review Board Statement: Not applicable.

Informed Consent Statement: Not applicable.

Data Availability Statement: All data supporting the findings of this study are available in an online repository (https://mda.vliz.be/directlink.php?fid=VLIZ_00000824_6339943796b93322139680).

Acknowledgments: The authors thank the captain and crew onboard R/V XIANG YANG HONG SHI HAO.

Conflicts of Interest: The authors declare no conflict of interest.

References

- Costa, K.M.; Anderson, R.F.; McManus, J.F.; Winckler, G.; Middleton, J.L.; Langmuir, C.H. Trace element (Mn, Zn, Ni, V) and authigenic uranium (aU) geochemistry reveal sedimentary redox history on the Juan de Fuca Ridge, North Pacific Ocean. *Geochim. Et Cosmochim. Acta* **2018**, *236*, 79–98. [[CrossRef](#)]
- Thomas, N.C.; Bradbury, H.J.; Hodell, D.A. Changes in North Atlantic deep-water oxygenation across the Middle Pleistocene transition. *Science* **2022**, *377*, 654–659. [[CrossRef](#)]
- Jaccard, S.L.; Galbraith, E.D.; Martínez-García, A.; Anderson, R.F. Covariation of deep Southern Ocean oxygenation and atmospheric CO₂ through the last ice age. *Nature* **2016**, *530*, 207–210. [[CrossRef](#)]
- Auderset, A.; Moretti, S.; Taphorn, B.; Ebner, P.-R.; Kast, E.; Wang, X.T.; Schiebel, R.; Sigman, D.M.; Haug, G.H.; Martínez-García, A. Enhanced ocean oxygenation during Cenozoic warm periods. *Nature* **2022**, *609*, 77–82. [[CrossRef](#)]
- Zachos, J.; Pagani, M.; Sloan, L.; Thomas, E.; Billups, K. Trends, Rhythms, and Aberrations in Global Climate 65 Ma to Present. *Science* **2001**, *292*, 686–693. [[CrossRef](#)]
- Hodell, D.A.; Venz, K.A.; Charles, C.D.; Ninnemann, U.S. Pleistocene vertical carbon isotope and carbonate gradients in the South Atlantic sector of the Southern Ocean. *Geochem. Geophys. Geosystems* **2003**, *4*, 1–19. [[CrossRef](#)]
- Hodell, D.A.; Venz-Curtis, K.A. Late Neogene history of deepwater ventilation in the Southern Ocean. *Geochem. Geophys. Geosystems* **2006**, *7*, Q09001. [[CrossRef](#)]
- Mackensen, A.; Schmiedl, G. Stable carbon isotopes in paleoceanography: Atmosphere, oceans, and sediments. *Earth-Sci. Rev.* **2019**, *197*, 102893. [[CrossRef](#)]
- Spero, H.J.; Bijma, J.; Lea, D.W.; Bemis, B.E. Effect of seawater carbonate concentration on foraminiferal carbon and oxygen isotopes. *Nature* **1997**, *390*, 497–500. [[CrossRef](#)]
- Zhang, J.; Quay, P.D.; Wilbur, D.O. Carbon isotope fractionation during gas-water exchange and dissolution of CO₂. *Geochim. Et Cosmochim. Acta* **1995**, *59*, 107–114. [[CrossRef](#)]
- Yi, L.; Xu, D.; Jiang, X.; Ma, X.; Ge, Q.; Deng, X.; Wang, H.; Deng, C. Magnetostratigraphy and Authigenic 10Be/9Be Dating of Plio-Pleistocene Abyssal Surficial Sediments on the Southern Slope of Mariana Trench and Sedimentary Processes During the Mid-Pleistocene Transition. *J. Geophys. Res. Ocean.* **2020**, *125*, e2020JC016250. [[CrossRef](#)]
- Yi, L.; Medina-Elizalde, M.; Tan, L.; Kemp, D.B.; Li, Y.; Kletetschka, G.; Xie, Q.; Yao, H.; He, H.; Deng, C.; et al. Plio-Pleistocene deep-sea ventilation in the Eastern Pacific and potential linkages with Northern Hemisphere glaciation. *Sci. Adv.* **2023**, *9*, eadd1467. [[CrossRef](#)] [[PubMed](#)]
- Jaccard, S.L.; Hayes, C.T.; Martínez-García, A.; Hodell, D.A.; Anderson, R.F.; Sigman, D.M.; Haug, G.H. Two Modes of Change in Southern Ocean Productivity Over the Past Million Years. *Science* **2013**, *339*, 1419–1423. [[CrossRef](#)]
- Dou, Y.; Yang, S.; Li, C.; Shi, X.; Liu, J.; Bi, L. Deepwater redox changes in the southern Okinawa Trough since the last glacial maximum. *Prog. Oceanogr.* **2015**, *135*, 77–90. [[CrossRef](#)]
- Wang, H.; Yi, L.; Deng, X.; He, G. Geochemical and Mineral Properties of Quaternary Deep-Sea Sediments in the Central-Tropical Pacific and Its Response to the Mid-Pleistocene Transition. *J. Mar. Sci. Eng.* **2021**, *9*, 1254. [[CrossRef](#)]
- van de Fliertdt, T.; Frank, M. Neodymium isotopes in paleoceanography. *Quat. Sci. Rev.* **2010**, *29*, 2439–2441. [[CrossRef](#)]
- Elderfield, H.; Ferretti, P.; Greaves, M.; Crowhurst, S.; McCave, I.N.; Hodell, D.; Piotrowski, A.M. Evolution of Ocean Temperature and Ice Volume Through the Mid-Pleistocene Climate Transition. *Science* **2012**, *337*, 704–709. [[CrossRef](#)]
- Pöppelmeier, F.; Lippold, J.; Blaser, P.; Gutjahr, M.; Frank, M.; Stocker, T.F. Neodymium isotopes as a paleo-water mass tracer: A model-data reassessment. *Quat. Sci. Rev.* **2022**, *279*, 107404. [[CrossRef](#)]
- Kruiver, P.P.; Passier, H.F. Coercivity analysis of magnetic phases in sapropel S1 related to variations in redox conditions, including an investigation of the S ratio. *Geochem. Geophys. Geosystems* **2001**, *2*, 2001GC000181. [[CrossRef](#)]
- Chang, L.; Bolton, C.T.; Dekkers, M.J.; Hayashida, A.; Heslop, D.; Krijgsman, W.; Kodama, K.; Paterson, G.A.; Roberts, A.P.; Rohling, E.J.; et al. Asian monsoon modulation of nonsteady state diagenesis in hemipelagic marine sediments offshore of Japan. *Geochem. Geophys. Geosystems* **2016**, *17*, 4383–4398. [[CrossRef](#)]
- Kissel, C.; Laj, C.; Jian, Z.; Wang, P.; Wandres, C.; Rebolledo-Vieyra, M. Past environmental and circulation changes in the South China Sea: Input from the magnetic properties of deep-sea sediments. *Quat. Sci. Rev.* **2020**, *236*, 106263. [[CrossRef](#)]
- Funk, J.A.; Dobeneck, T.v.; Reitz, A. Integrated Rock Magnetic and Geochemical Quantification of Redoxomorphic Iron Mineral Diagenesis in Late Quaternary Sediments from the Equatorial Atlantic. In *The South Atlantic in the Late Quaternary*; Wefer, G., Mulitza, S., Ratmeyer, V., Eds.; Springer: Berlin/Heidelberg, Germany, 2004; pp. 237–260.
- Korff, L.; von Dobeneck, T.; Frederichs, T.; Kasten, S.; Kuhn, G.; Gersonde, R.; Diekmann, B. Cyclic magnetite dissolution in Pleistocene sediments of the abyssal northwest Pacific Ocean: Evidence for glacial oxygen depletion and carbon trapping. *Paleoceanography* **2016**, *31*, 600–624. [[CrossRef](#)]
- Kars, M.; Musgrave, R.J.; Kodama, K.; Jonas, A.-S.; Bordiga, M.; Ruebsam, W.; Mleneck-Vautraviers, M.J.; Bauersachs, T. Impact of climate change on the magnetic mineral assemblage in marine sediments from Izu rear arc, NW Pacific Ocean, over the last 1Myr. *Palaeogeogr. Palaeoclimatol. Palaeoecol.* **2017**, *480*, 53–69. [[CrossRef](#)]
- Shin, J.Y.; Yu, Y.; Seo, I.; Hyeong, K.; Lim, D.; Kim, W. Magnetic Properties of Deep-Sea Sediments From the North Pacific: A Proxy of Glacial Deep-Water Ventilation. *Geochem. Geophys. Geosystems* **2018**, *19*, 4433–4443. [[CrossRef](#)]
- Roberts, A.P. Magnetic mineral diagenesis. *Earth-Sci. Rev.* **2015**, *151*, 1–47. [[CrossRef](#)]

27. Ge, K.; Williams, W.; Liu, Q.; Yu, Y. Effects of the core-shell structure on the magnetic properties of partially oxidized magnetite grains: Experimental and micromagnetic investigations. *Geochem. Geophys. Geosystems* **2014**, *15*, 2021–2038. [[CrossRef](#)]
28. Jackson, M.; Worm, H.-U.; Banerjee, S.K. Fourier analysis of digital hysteresis data: Rock magnetic applications. *Phys. Earth Planet. Inter.* **1990**, *65*, 78–87. [[CrossRef](#)]
29. Heslop, D. Numerical strategies for magnetic mineral unmixing. *Earth-Sci. Rev.* **2015**, *150*, 256–284. [[CrossRef](#)]
30. Heslop, D.; Roberts, A.P. Unmixing Magnetic Hysteresis Loops. *J. Geophys. Res. Atmos.* **2012**, *117*, 3758. [[CrossRef](#)]
31. Maher, B.A. Magnetic properties of some synthetic sub-micron magnetites. *Geophys. J.* **1988**, *94*, 83–96. [[CrossRef](#)]
32. Duan, Z.; Gao, X.; Liu, Q. Anhyseretic remanent magnetization (ARM) and its application to geoscience. *Prog. Geophys.* **2012**, *27*, 1929–1938. [[CrossRef](#)]
33. Evans, M.E.; Heller, F. *Environmental Magnetism: Principles and Applications of Enviromagnetics*; Academic Press: New York, NY, USA, 2003; p. 322.
34. van Haren, H.; Berndt, C.; Klaucke, I. Ocean mixing in deep-sea trenches: New insights from the Challenger Deep, Mariana Trench. *Deep Sea Res. Part I Oceanogr. Res. Pap.* **2017**, *129*, 1–9. [[CrossRef](#)]
35. Xiao, C.; Wang, Y.; Tian, J.; Wang, X.; Xin, Y. Mineral composition and geochemical characteristics of sinking particles in the Challenger Deep, Mariana Trench: Implications for provenance and sedimentary environment. *Deep Sea Res. Part I Oceanogr. Res. Pap.* **2020**, *196*, 104373. [[CrossRef](#)]
36. Yi, L.; Hu, B.; Zhao, J.; Jiang, X.; Shu, Y.; Wang, X.; Guo, J.; Wang, F.; Ding, X.; Liu, G.; et al. Magnetostratigraphy of Abyssal Deposits in the Central Philippine Sea and Regional Sedimentary Dynamics During the Quaternary. *Paleoceanogr. Paleoclimatology* **2022**, *37*, e2021PA004365. [[CrossRef](#)]
37. Yi, L.; Wang, H.; Deng, X.; Yuan, H.; Xu, D.; Yao, H. Geochronology and Geochemical Properties of Mid-Pleistocene Sediments on the Caiwei Guyot in the Northwest Pacific Imply a Surface-to-Deep Linkage. *J. Mar. Sci. Eng.* **2021**, *9*, 253. [[CrossRef](#)]
38. Yamazaki, T. Environmental magnetism of Pleistocene sediments in the North Pacific and Ontong-Java Plateau: Temporal variations of detrital and biogenic components. *Geochem. Geophys. Geosystems* **2009**, *10*, Q07Z04. [[CrossRef](#)]
39. Yamazaki, T. Paleoposition of the Intertropical Convergence Zone in the eastern Pacific inferred from glacial-interglacial changes in terrigenous and biogenic magnetic mineral fractions. *Geology* **2012**, *40*, 151–154. [[CrossRef](#)]
40. Day, R.; Fuller, M.; Schmidt, V.A. Hysteresis properties of titanomagnetites: Grain-size and compositional dependence. *Phys. Earth Planet. Inter.* **1977**, *13*, 260–267. [[CrossRef](#)]
41. Maxbauer, D.P.; Feinberg, J.M.; Fox, D.L. MAX UnMix: A web application for unmixing magnetic coercivity distributions. *Comput. Geosci.* **2016**, *95*, 140–145. [[CrossRef](#)]
42. Dunlop, D.J. Theory and application of the Day plot (Mrs/Ms versus Hcr/Hc) 1. Theoretical curves and tests using titanomagnetite data. *J. Geophys. Res. Solid Earth* **2002**, *107*, EPM 4-1-EPM 4-22. [[CrossRef](#)]
43. Dunlop, D.J. Theory and application of the Day plot (Mrs/Ms versus Hcr/Hc) 2. Application to data for rocks, sediments, and soils. *J. Geophys. Res. Solid Earth* **2002**, *107*, EPM 5-1-EPM 5-15. [[CrossRef](#)]
44. Roberts, A.P.; Heslop, D.; Zhao, X.; Pike, C.R. Understanding fine magnetic particle systems through use of first-order reversal curve diagrams. *Rev. Geophys.* **2014**, *52*, 557–602. [[CrossRef](#)]
45. Roberts, A.P.; Pike, C.R.; Verosub, K.L. First-order reversal curve diagrams: A new tool for characterizing the magnetic properties of natural samples. *J. Geophys. Res. Solid Earth* **2000**, *105*, 28461–28475. [[CrossRef](#)]
46. Deng, X.; Yi, L.; Paterson, G.A.; Qin, H.; Wang, H.; Yao, H.; Ren, J.; Ge, J.; Xu, H.; Deng, C.; et al. Magnetostratigraphic evidence for deep-sea erosion on the Pacific Plate, south of Mariana Trench, since the middle Pleistocene: Potential constraints for Antarctic bottom water circulation. *Int. Geol. Rev.* **2016**, *58*, 49–57. [[CrossRef](#)]
47. Li, J.; Liu, Y.; Liu, S.; Roberts, A.P.; Pan, H.; Xiao, T.; Pan, Y. Classification of a Complexly Mixed Magnetic Mineral Assemblage in Pacific Ocean Surface Sediment by Electron Microscopy and Supervised Magnetic Unmixing. *Front. Earth Sci.* **2020**, *8*, 609058. [[CrossRef](#)]
48. Yi, L.; Wang, H.; Liu, G.; Chen, Y.; Yao, H.; Deng, X. Magnetic minerals in Mid-Pleistocene sediments on the Caiwei Guyot, Northwest Pacific and their response to the Mid-Brunhes climate event. *Acta Oceanol. Sin.* **2021**, *40*, 1–11. [[CrossRef](#)]
49. Roberts, A.P.; Tauxe, L.; Heslop, D.; Zhao, X.; Jiang, Z. A Critical Appraisal of the “Day” Diagram. *J. Geophys. Res. Solid Earth* **2018**, *123*, 2618–2644. [[CrossRef](#)]
50. Özdemir, Ö.; Dunlop, D.J. Hallmarks of maghemitization in low-temperature remanence cycling of partially oxidized magnetite nanoparticles. *J. Geophys. Res. Solid Earth* **2010**, *115*, B02101. [[CrossRef](#)]
51. Yao, H.; Wang, F.; Wang, H.; Yu, M.; Ren, J.-b.; He, G.; Chen, W.; Yi, L. Pleistocene magnetostratigraphy of four cores in the West Philippine Basin and regional sedimentary shift during the Mid-Pleistocene Transition. *Geol. J.* **2021**, *56*, 2919–2929. [[CrossRef](#)]

Disclaimer/Publisher’s Note: The statements, opinions and data contained in all publications are solely those of the individual author(s) and contributor(s) and not of MDPI and/or the editor(s). MDPI and/or the editor(s) disclaim responsibility for any injury to people or property resulting from any ideas, methods, instructions or products referred to in the content.